nature communications

Article

https://doi.org/10.1038/s41467-025-68139-9

Perpendicular neuromorphic channels facilitate lateral inhibition for tactile location

Received: 27 November 2024

Accepted: 19 December 2025

Published online: 07 January 2026

Check for updates

Lu Liu[1,2,3], Yao Ni[1,2,3], Honghuan Xu[1,2,3], Yiming Yuan[1,2] & Wentao Xu[1,2]

Lateral inhibition refers to the inhibition of neurons as caused by excitation of its neighboring neurons, which helps increase the contrast and sharpness of touch, and pinpoint exact touch position. However, such important operational logic has not yet been realized in neuromorphic sensing systems at the device level. Herein, we demonstrate a cross-channel synaptic transistor (CST) that possesses two perpendicularly-integrated channels with separate source and drain electrodes but the same geometrical middle points. The architecture is fabricated by electro-hydrodynamically printed indium zinc oxide (IZO) nanowires with digital control. When one channel is excited, it attenuates the charge-carrier transport in its perpendicular channel, fundamentally realizing the lateral inhibition behavior on the device level, forming a competitive charge-transport mechanism. The device was successfully applied to precise localization of the touch point on an electronic skin, and the position can be visually displayed simultaneously. The special device architecture can be used to generate a lateral-inhibition-encryption (LIE) key that encrypts Morse code, which ensures 100% accurate decryption by traversal decryption of all letters and encryption types. This work demonstrates a new strategy to emulate bioinspired operation logic on device level for the construction of future bioinspired electronics.

When our skin is subjected to a sudden touch at some point, our event-driven neural information processing can precisely pick out this information from a variety of tactile information[1–7]. This frequently occurs in our daily life, essential for tremendous everyday tasks[8–10]. The precise localization of touch attributes to lateral inhibition, which is an important neural processing mechanism that refers to the excitable activities of a neuron upon stimulation results in inhibitory effects on neighboring neurons[11,12]. Lateral inhibition enhances the accuracy of perception, recognition, and spatial localization of stimuli by reducing the response of peripheral neurons by reducing background noise and interference[13–15]. Lateral inhibition mechanism has inspired a variety of research fields, for improving the functions of artificial senses[16–18].

Lateral inhibition is applicable to a variety of bioinspired applications[19]. In artificial intelligence, "algorithmic lateral inhibition" assists neural networks to focus visual attention for objective recognition[20], real-time motion recognition[21]. This mechanism also inspires some preliminary research on functional device sets for constructing visual processing. Different terminals in the same synaptic transistor are used to emulate the competition between horizontal cells, by employing the lateral gates of an anti-ferroelectric field-effect transistor[22]. Other attempts include the combination of a controlling transistor with a sensing unit, where light and olfactory responses are inhibited by tuning the gate voltage inputs to restrict the charge injected into the parasitic drain capacitor of the sensor unit[23,24]. However, these implementations of lateral inhibition either rely on the

[1]Institute of Photoelectronic Thin Film Devices and Technology, Key Laboratory of Optoelectronic Thin Film Devices and Technology of Tianjin, College of Electronic Information and Optical Engineering, Engineering Research Center of Thin Film Photoelectronic Technology of Ministry of Education, Academy for Advanced Interdisciplinary Studies, Nankai University, Tianjin, China. [2]Shenzhen Research Institute of Nankai University, Shenzhen, China. [3]These authors contributed equally: Lu Liu, Yao Ni, Honghuan Xu. e-mail: wentao@nankai.edu.cn

https://doi.org/10.1038/s41467-025-68139-9

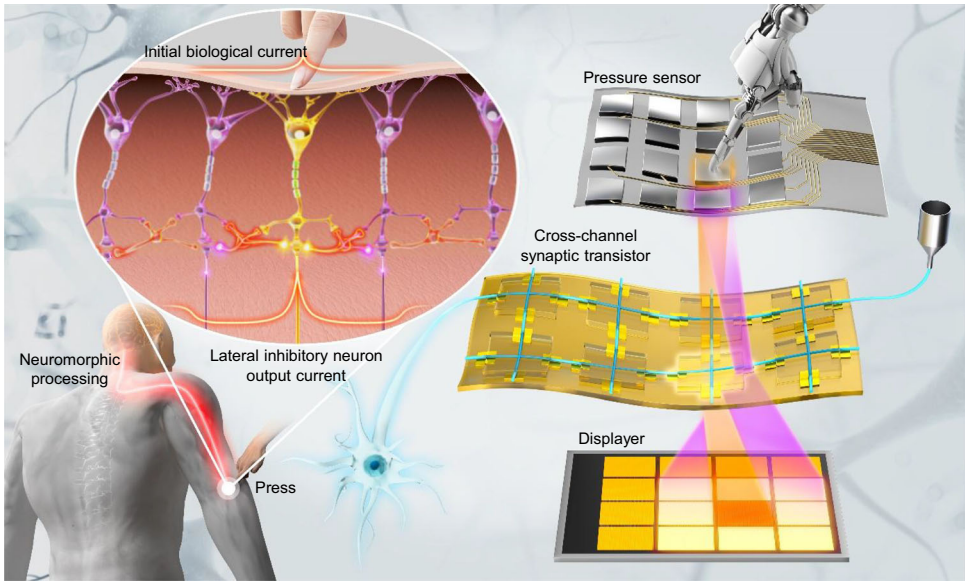

Fig. 1 | Schematic of biological and artificial tactile nervous systems with lateral inhibition mechanism. (left) A biological afferent nervous system, with enhanced sense of touch by lateral inhibition. (right) An artificial tactile nervous system that implements lateral inhibition to process tactile information, with simultaneous visual display.

inherent properties of conventional transistors that require manual intervention for inhibitory stimulus regulation, or they depend on the collaboration of different types of functional modules, which do not represent inhibitory effect between similar neurons, and thus difficult to fully replicate the complete functionality of biological lateral inhibition. All the above processes are modulated by artificial electrical pulses, whereas lateral inhibition is usually caused by the sense of surrounding environment to result in the inhibitory effect. Moreover, further exploration is needed on how lateral inhibition assists tactile perception in electronic skin, which is essential in constructing bioinspired and bio-integrated interfaces.

Herein, we demonstrate a tactile nervous system that involves lateral inhibition behavior, for precise localization of tactile information, which is also visually displayed simultaneously. This is realized by a specially designed key information processing unit, a cross-channel synaptic transistor (CST) with two crossed indium zinc oxide (IZO) nanowires as perpendicular but jointed channel as digitally printed by electrohydrodynamic nanowire printing technique, gated by a shared ion gel sheet. When one channel is excited, the other channel is laterally attenuated, serving as the inhibitory channel and implying lateral inhibition. CST was used to develop a lateral inhibition key for secure communication with 100% decryption accuracy. This work offers a new insight to the construction of bioinspired systems and electronics.

Results

Design concept

When our skin is touched, several adjacent receptors can be activated[25]. A layer of interneurons between sensory cells and neurons leading to the central nervous system can transmit excitatory signals from receptor cells, and send inhibitory signals to other nearby interneurons, to concentrate our focus on the central contact region. This phenomenon is known as lateral inhibition[26,27]. We demonstrate an artificial tactile nervous system that is composed of cross-channel synaptic transistors to replicate the above phenomenon. We fabricated a pair of perpendicularly aligned IZO nanowires (NWs) for the synaptic transistors using electrohydrodynamic nanowire printing (e-NWP) process, and used the device to process the perceived tactile information, which is centralized by the lateral inhibition mechanism and simultaneously displayed visually (Fig. 1).

Design and fabrication of CST

A CST with perpendicular IZO-channels was fabricated to demonstrate the lateral inhibition phenomenon (Fig. 2a): A tungsten probe in contact with ion gel emulated the biological axon and presynaptic membrane to conduct presynaptic spikes. The ion gel rich in mobile ions that could migrate to the channel region in response to the presynaptic spike, inducing the change of charge carrier amounts in the channels. One of the IZO channels emulated synaptic cleft, through which neurotransmitters are released to cause postsynaptic currents (PSC) as controlled by resting potential (V_{DS1}) of 1 V and the stimulation potential (V_{GS}). The other IZO channel served as the laterally inhibitory side, receiving information from neighboring neurons through the second drain.

Digitally-aligned long and continuous IZO NWs were printed using e-NWP, which is a cost-effective, eco-friendly and precise printing technique[28]. Cross-structured NW arrays were mass produced, showing high transparency (Fig. 2b). The NW arrays exhibited a straight and uniform morphology with consistent diameters (Fig. 2c, d), and the spacing between the arrays was precisely controlled, with a minimum spacing of 20 μm (Fig. 2e–h). The intersections of the NWs changed from a stacked to a flat morphology after sintering (Fig. 2i,j). The typical diameter of a single NW was ~250 nm (Fig. 2k). Elemental mapping demonstrated the evenly distributed indium (In), zinc (Zn), and oxygen (O) in a NW (Fig. 2l).

Sensory cells can improve acuity through the lateral inhibition mechanism[29]. When there is overlap of receptive fields, this mechanism works. A single stimulus, *e.g.*, slight press of a pencil tip on skin, can activate several adjacent receptors near the tip. Normally, all these cells might pass on a stimulatory message to the central nervous system, making it difficult to determine the exact location of the touch point. However, if lateral inhibition is applicable, then there is a layer of interneurons that lie between the sensory cells and the neurons that lead to the central nervous system. These interneurons relay excitatory signals from the receptor cells, but they also employ axonal branches that can send inhibitory signals to other interneurons nearby. This set up allows the interneuron that receives the strongest signal from a sensory cell to amplify the stimulatory message to the central nervous system while inhibiting the signals from nearby interneurons[30]. As a result, the signal to the central nervous system is more focused

https://doi.org/10.1038/s41467-025-68139-9

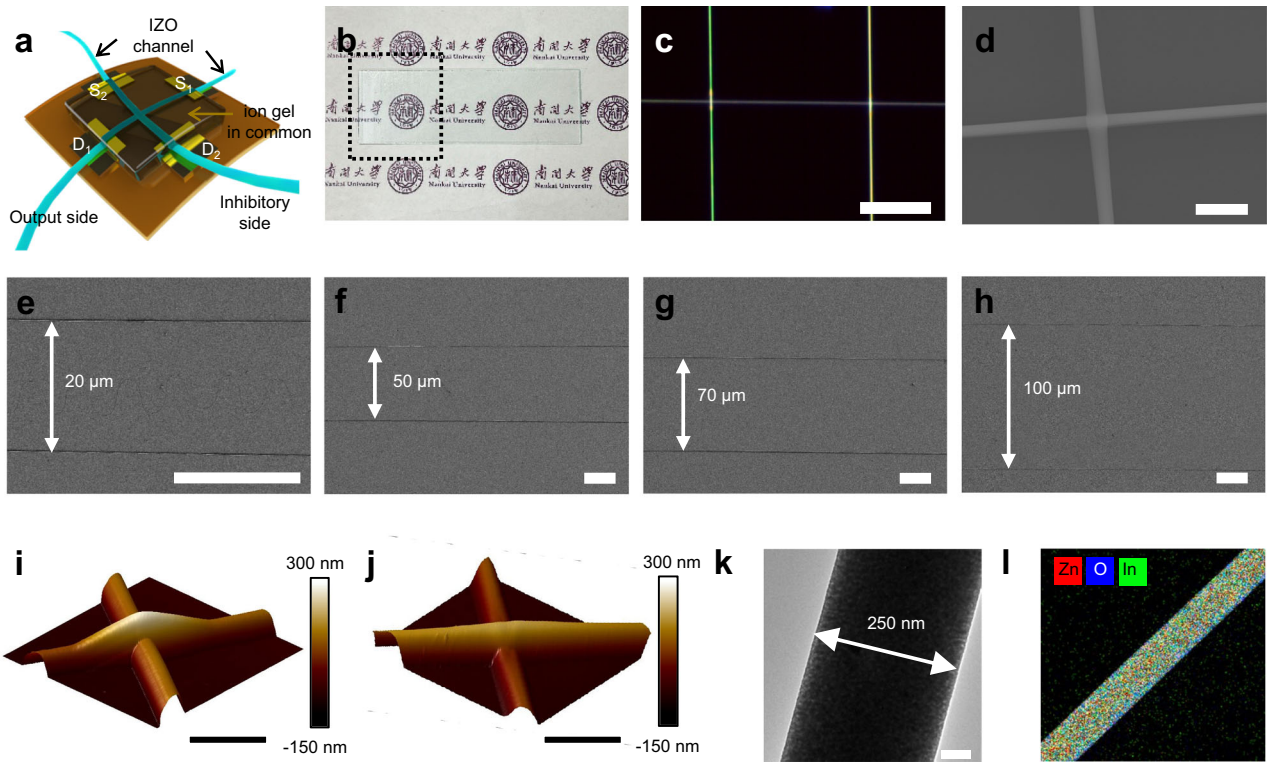

Fig. 2 | Characterization of the cross channels. a Schematic of CST with IZO cross-channels, gated by a shared ion gel thin film. **b** Photograph and (**c**) OM image of crossed IZO NW arrays. Scale bars, 10 μm. **d** SEM image of crossed IZO NWs. Scale bars, 10 μm. **e**–**h** SEM image of IZO NWs array with different spacing. Scale bars, 20 μm. AFM images of crossed IZO NWs (**i**) before and (**j**) after calcination. Scale bars, 1 μm. **k** TEM image of IZO NWs as printed on copper gauze. Scale bars, 50 nm. **l** Elemental mapping of indium, zinc, and oxygen in IZO NWs.

(Fig. 3a). Similar phenomenon was simulated by CST. When the applied lateral inhibition voltage (V_{DS2}) increased, the transfer curves of inhibitory side showed potentiation trend, while output attenuation trend (Supplementary Fig. S1a–c and Fig. S2). Under shared top gate, the gate current was significantly smaller than the channel current (Supplementary Fig. S1d). To elucidate the lateral-inhibition mechanism, finite-element simulations of the electric-field (Supplementary Fig. S3a) and potential distributions (Supplementary Fig. S3b) were performed under varied V_{DS2}, confirming the progressive suppression of the output side and the eventual reversal of the inhibitory channel current. When applied single presynaptic spike (4 V, 50 ms), PSCs were induced to simulate transmission of neurotransmitters in the synaptic cleft. With the increase of V_{DS2}, PSC from output side exhibited an attenuation of amplitude (Supplementary Fig. S4).

As an essential type of short-term plasticity (STP), paired-pulse facilitation (PPF) plays a pivotal role in neural information processing. Its functionalities encompass the transmission of information across synapses and the temporal filtering of bioinformation, etc.[31–36]. The CST has replicated the functionality of PPF. Two consecutive presynaptic spikes (4 V, 50 ms) were applied under different V_{DS2}, the first spike induced an action response A_1, and the second produced a response A_2, the interval time Δt between the two spikes was 50 ms. PPF index (100% × A_2/A_1) of output side were calculated as 155.27%, 153.83%, 163.88% and 159.03% when under V_{DS2} of 0, 0.2, 0.5 and 1 V, which certified that the application of lateral inhibition only changes the amplitude of PSCs but has negligible effect on the plasticity (Supplementary Fig. S5).

Figure 3b illustrates the PSC of the output side in CST under no lateral inhibition (V_{DS2} = 0 V) and with lateral inhibition (V_{DS2} = 1 V). Despite the enhancement of PSC after 20 presynaptic spikes of 4 V in both cases, the synaptic input from the inhibitory side results in a significant attenuation of the amplitude compared to the synapse without lateral inhibition. Furthermore, through the drain terminal of the inhibitory side, PSC originating from the inhibitory side can also be observed (Fig. 3c). The patterns of enhancement and attenuation were opposite to those observed in the PSC from the output side, in accordance with Kirchhoff's current law (KCL)[37]. This provides additional synaptic weight evidence for tracking changes in data within the internal system.

Suppressive input of different intensities from inhibitory side can regulate synaptic weights in response to fixed spikes. We investigated the inhibitory-strength-dependent plasticity of CST by varying V_{DS2} ranging from 0 to 1 V. As the inhibitory voltage increased, the output PSC peak showed a nearly linear reduction, with a maximum reduction of 43% compared to the non-inhibited state within this range (Supplementary Fig. S6). To further quantify the influence of V_{DS2} on the temporal dynamics of synaptic plasticity, the PSC-retention curves were fitted using a simple first-order stretched exponential function (SEF)[38]:

$$I = (I_0 - I_\infty) \times \exp[-(t/\tau - t_0/\tau)^\beta] + I_\infty \quad (1)$$

where t_0 is the time that the pulse finishes, I_0 is the initial PSC when the presynaptic spike finishes, I_∞ is the final PSC at equilibrium, $0 \le \beta \le 1$ is a stretch index, and τ is the retention time. In the CST, as V_{DS2} increases from 0 to 1 V, τ initially decreases and then increases, forming an approximately symmetric relationship around the inhibitory voltage of 0.5 V. The fluctuation range of τ value is not significant, which is attributed to the two perpendicular IZO-channels sharing the same gate, thereby ensuring comparable synaptic plasticity in these channels (Supplementary Fig. S7). The device was tested under different humidity from 20% to 60%, and back to 20% (Supplementary Fig. S8).

The electric field and current distribution in CST were simulated using COMSOL Multiphysics (Fig. 3g–j)[39], where the arrow size and

https://doi.org/10.1038/s41467-025-68139-9

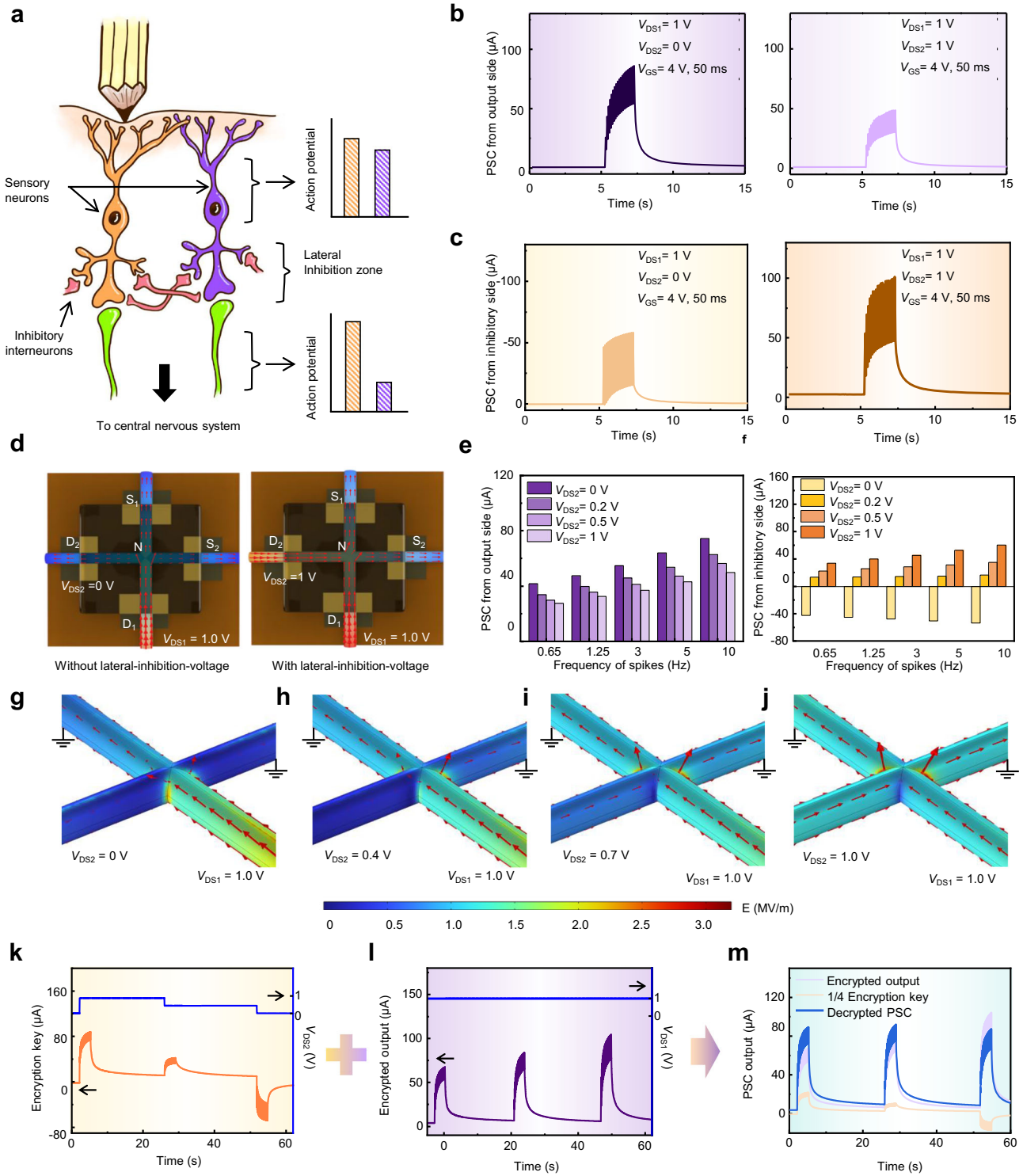

Fig. 3 | Electrical properties of the five-terminal cross-channel device. **a** Schematic diagram of tactile lateral inhibition. PSC from **b** the output side and **c** the inhibitory side triggered by 20 consecutive presynaptic spikes (4 V, 50 ms) without and with lateral inhibition. **d** Electric-field schematics of CST without and with lateral-inhibition voltage. Histograms of PSC from **e** the output side and **f** the inhibitory side triggered by different frequency of presynaptic spikes under different inhibitory voltages. Electric field and current distributions in IZO-NWs under V_{DS2} = **g** 0, **h** 0.4, **i** 0.7, and **j** 1 V at the simulation time of 2 s. PSC outputs from **k** the inhibitory side, **l** the output side, and **m** the decryption weighted PSC in secure communication.

direction represent the magnitude and direction of the current in the NWs at the simulation time of 2 s, respectively. The electric field and current distributions under different V_{DS2} were consistent with the trend in PSC (Supplementary Fig. S9). Current-voltage (*I-V*) contour maps from output side and from inhibitory side elucidates the operation mechanism of the CST with IZO cross-channels (Supplementary Fig. S10).

Furthermore, a series of spike trains at different frequencies were applied to investigate frequency-dependent plasticity under the influence of different levels of lateral inhibition (Supplementary

Fig. S11). As the pulse frequency increased, both PSCs from the output side and inhibitory side increased (Fig. 3e, f); this was due to the high-frequency stimulation driving more cations to migrate towards the channel region, inducing larger electron flow[40]. Through the synergistic interaction of spike frequency and inhibitory voltage, the regulatory range of synaptic weights on the output side could be increased by up to 270% (Fig. 3e). Moreover, when a sufficiently large bias voltage of 1 V was applied by the inhibitory side, it caused an inversion of the output PSC of this side (Fig. 3f). A similar phenomenon was observed for PSCs triggered by presynaptic stimuli with different numbers of spikes (Supplementary Fig. S12). This characteristic can be utilized in signal processing applications to determine whether sufficient lateral inhibition is present simply by assessing the polarity of the PSC[41].

We validated the processing capability of CST in response to stimulus signals by applying a series of alternating inhibitory pulses at 0 V and 1 V. It was observed that the polarity of the inhibitory-side PSC switched instantly with the variation of inhibitory bias voltage (Supplementary Fig. S13b). Furthermore, unlike the conventional approach of modulating synaptic weights through applied gate spikes, the output-side PSC was regulated by the inhibitory bias voltage, achieving potentiation-depression regulation (Supplementary Fig. S13a). This provides a new approach for synaptic weight update. After over 150 cycles of testing, CST exhibited stable PSC of a negligible decay, indicating its great encoding potential.

The response speed of output side and inhibitory side was measured, showing a rise period (t_{on}) of 39.9 ms, 42.2 ms and a drop period (t_{off}) of 656.8 ms, 43.3 ms, respectively (Supplementary Fig. S14). The extended t_{off} is a result of the synaptic plasticity in the device, which is essential for in-sensor information processing. Energy consumption of the device is evaluated as $E = AIW$, where A is driving voltage, I is channel current, and W is duration of presynaptic spike. For a single channel, the minimal E of output side was ~0.108 fJ per synaptic event, with $A = 0.01$ mV, $I = 0.215$ nA, and $W = 50$ ms (Supplementary Fig. S15a). Spike-number-dependent plasticity (SNDP) was also emulated using consecutive presynaptic spikes (Supplementary Fig. S15b). Applying a consecutive sequence of presynaptic spikes to CST, the stimulus enhancement from the inhibitory side and the attenuation from the output side (Supplementary Fig. S16) significantly improves the ratio between EPSC, which contributes to the differential processing between pixels. The wafer-level device fabrication process to verify the scalability of the cross-channel printing process (Supplementary Fig. S17). The nanowire array-based CST had a device pitch of 180 μm (Supplementary Fig. S18). The electrical properties of the CST are compared with state-of-art lateral inhibition-based neuromorphic systems (Table S1)[22,23,42–45]. The cross-coupled nanowire architecture of CST encodes data in the form that cannot be retrieved by a single channel, providing physically built-in information protection without extra encryption circuit. The device shows high energy-efficiency. The system could be improved by further improving the response time asymmetry and reducing the pitch size.

The uniformity of response across the CST array was systematically evaluated. Under identical presynaptic spikes (4 V, 50 ms) with lateral inhibition under $V_{DS2} = 0.5$ V, highly reproducible currents from output side and inhibitory side were observed across all 3 × 3 devices (Supplementary Fig. S19). The device-to-device (D2D) variations were examined using data statistics. The variation coefficient (σ/μ) for peak currents A_1, A_5, and A_{20} were calculated to be 4.09%, 3.57%, and 4.25% at the output side, and to be 2.57%, 2.16%, and 1.97% at the inhibitory side, respectively, where σ denotes the standard deviation and μ is the mean value (Supplementary Fig. S20).

We further investigated the application of CST in secure communication by applying different bias voltages to the inhibitory side. Using the PSC from inhibitory side as the encryption key (Fig. 3i) and the PSC from output side as the encrypted PSC (Fig. 3j), then the original PSC response without inhibitory bias can be reconstruct by weighting the two PSCs. Remarkably, even under different inhibitory states, the decryption method yielded highly accurate signal reconstruction compared to the unencrypted signal (Fig. 3k).

Encryption and decryption of Morse letters

The CST was used to respond to electrical impulses that represented international Morse code, and thereby demonstrated potential application in encrypted signal coding[46]. Stimulated by encoded short "dot" signals (4 V, 0.1 s) and long "dash" signals (4 V, 0.15 s), the CST efficiently generated distinct PSC amplitudes on the output side corresponding to English letters (Fig. 4a, b and Supplementary Fig. S21). Notably, the amplitude of the inhibition-encryption side PSC remained stable throughout the decoding process (Figs. 4a, b).

Additionally, due to its exclusive lateral inhibition function, CST can encrypt Morse letters by modulating the bias voltage on the inhibitory side, serving as the lateral-inhibition-encryption (LIE) key. The negative encryption key represents unencrypted, while positive one represents encrypted (Fig. 4c, left). This LIE method can suppress the large PSC peaks of representing "dash" signals to a level equivalent to the small peaks of short "dot" signals, thus Morse letters containing one or more "dash" signals can receive varying degrees of encryption (Fig. 4c, d). Using the letter "J" as an example, it can be transformed into 7 other encrypted signals by encrypting the "dash" signals in different positions (Fig. 4e). The total of 8 possible outputs makes it very challenging to trace back to their original signals without the LIE key. This method can increase the confidentiality of communication, potentially applicable to such as aviation lighthouses, to transmit information to aircraft, and provide solutions for setting the direction of information transmission in smart-home devices such as electronic locks. A confusion matrix in Fig. 4f summarizes the LIE of 26 letters. For letters containing only "dot" signals, they cannot be encrypted and only produce unique possible signals, with a low security level of only 1; As the number of "dash" signals increases, the potential output type after encryption also increases, with the security level progressively rising to a maximum of 8. Randomized encryption of phrase "nan kai" was also achieved by this method (Supplementary Fig. S22).

With the assistance and weighting of the encryption key (Fig. 3i–k), the encrypted letters can also be decrypted and the PSC peaks corresponding to 'dot' and 'dash' can be reconstructed (Fig. 4g). After traversing and decrypting all the letters and encryption types, it was verified that this method could achieve 100% accurate decryption (Fig. 4h). Compared with the state-of-the-art devices with encryption functions, CST not only achieves instantaneous large-signal transmission and encryption with just one single input, but also instantly outputs key signals through an additional lateral inhibition output, benefiting from the symmetric channels and the shared gate. Furthermore, owing to the unique characteristics of cross-coupled dual channels, CST represents the first instance where measurable key signals are weighted to achieve high-accuracy decryption (Table S2)[47–55].

Accurate Morse coding for the long sentence "I LOVE NEUROMORPHIC DEVICE" was achieved by representing combinations of "dot" and "dash" signals to represent different letters. Based on the LIE method, the original long sentence was randomly encrypted. By randomly suppressing the encryption key on the inhibitory side, each letter was randomly encrypted to generate an encrypted signal: "I LDHE IESSKNUSHHIB SEHIFE". Using decryption process to achieve lossless backtracking of the original contents of the encrypted signal (Fig. 4i). In addition, employing a 10 N pressure as an encryption key and utilizing the above described decryption procedure, the phrase "Nankai" was encrypted and decrypted effectively (Supplementary Fig. S23). This coding system based on lateral suppression encryption provided a secure encryption and decryption method, which protected the confidentiality of sensitive information. This system has

https://doi.org/10.1038/s41467-025-68139-9

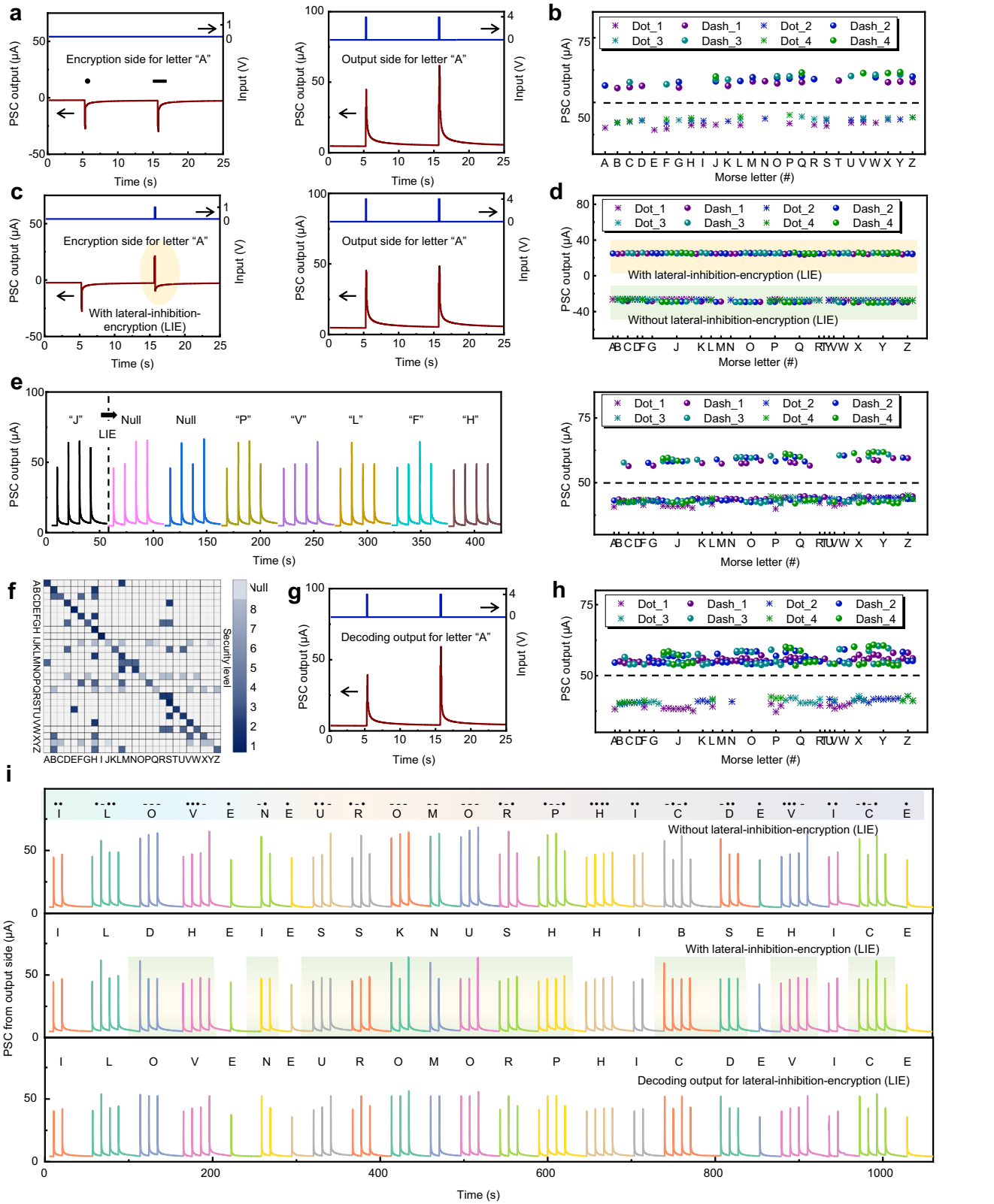

Fig. 4 | Encryption and decryption using a lateral-inhibition encryption (LIE) key. a Without an encryption, PSC from the encryption side and the output side representing the International Morse code of letter "A". **b** Without an encryption, output-side PSC distribution of 26 Morse letters. **c** With a LIE, PSC from the encryption side and the output side representing the International Morse code of letter "A". **d** With a LIE, encryption side and output-side PSC distribution from of 26 Morse letters. **e** PSC from 1 unencrypted output and 7 encrypted outputs of letter "J". **f** A confusion matrix of 26 letters under LIE processing. **g** After decryption, weighted PSC representing the International Morse code of letter "A". **h** After decryption, the weighted PSC distribution of 26 Morse letters. **i** With, without an encryption, and decoding output PSC from the encryption side and the output side representing the International Morse code of sentence "I love neuromorphic device".

https://doi.org/10.1038/s41467-025-68139-9

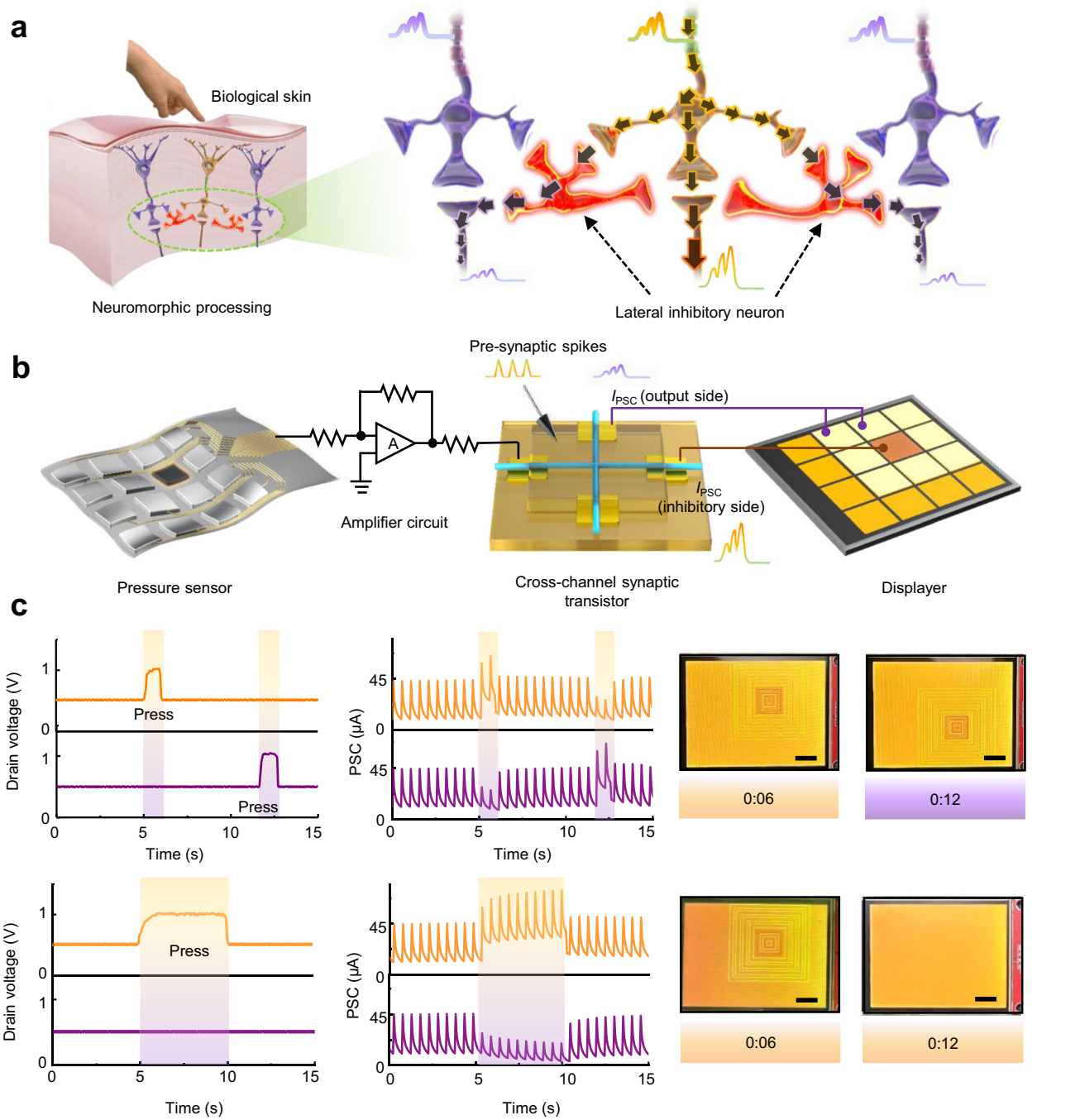

Fig. 5 | Lateral inhibition in an artificial tactile nervous system. a Schematic diagram of tactile information processing by lateral inhibitory neurons. **b** Schematic illustration of artificial tactile nervous system: pressure sensor, CST, signal processing module and displayer. **c** Drain voltage and PSC of CST triggered by pressing different positions of the pressure sensor, real-time picture of the displayer at different time nodes. Scale bars, 1 cm.

potential applications in protecting data security and privacy, potentially applicable to secure wearable devices, internet of things (IoT), etc.

Lateral inhibition in an artificial tactile nervous system

Under the effect of somatosensory lateral inhibition, when a skin region is stimulated, the unstimulated regions around it are also be affected, which can reduce the excitation level of the surrounding regions, thereby helping people perceive and localize the source of stimulation more accurately (Fig. 5a). To achieve this, an artificial tactile nervous system was fabricated to achieve real-time perception and signal processing of external stimuli at different locations under lateral inhibition, and to execute visual sensing of the stimulation location through display unit (Fig. 5b and Supplementary Fig. S24). In our tactile nervous system, pressure signals acting at different locations were captured and converted into electrical signals by the responding pressure-sensitive units as bias voltages applied to the inhibitory side of CST. In this process, PSC on the inhibitory side increased, representing an increase in pressure in the center region, and the PSC on the output side decreased, representing that the surrounding region was affected to present an inhibitory effect. PSC was converted to voltage by the amplification module, read by the control module, and transmitted to the display unit through the display encoding to visualize and locate the pressure lateral inhibition.

People can accurately locate stimuli on the skin through lateral inhibition. Analogously, for our tactile nervous system, when different position units of the sensor are pressed with pressures up to 10 N, the bias voltage of the inhibitory side of the CST increases from 0.5 to 1 V, peak values of the PSC of the output side and inhibitory side change from 45 μA, controlling the change of the color of the display unit. When pressed one sensitive unit, PSC on the inhibitory side rapidly increased to ~66 μA, PSC on the output side decreased to ~25 μA, the color of the corresponding unit of the display device deepened, and the color of the surrounding area became lighter (event #1, 6 s). When pressed the adjacent pressure-sensitive unit, the color change at another location was accurately displayed (event #2, 12 s). When continuously pressed the pressure-sensitive unit, PSC of the inhibitory side continued to increase, the color of the display area deepened (event #3, 6 s). When the pressure is released, PSC quickly returned to the initial state, the display device restored (event #4, 12 s) (Fig. 5c). In addition, calibration curves of ΔPSCs under various pressures were constructed to discern the impact of pressure magnitude (Figure S25). This lateral inhibition mechanism facilitates more accurate touch localization. (Supplementary Fig. S26).

Additionally, to enhance the robustness of our LIE-based encryption/decryption strategy against device non-idealities, we integrated it with a reservoir computing process (Supplementary Fig. S27a). We introduced random sampling offsets of ±0.15 s and ±3% noise into the signals, creating a training set with 2058 non-ideal samples (Supplementary Fig. S27b). The LIE-RC system achieved 100% recognition accuracy, demonstrating its strong compensatory capabilities and potential for adaptive calibration under non-ideal conditions (Supplementary Fig. S27c).

Discussion

We fabricated an artificial tactile nervous system that replicates the lateral inhibition mechanism in human skin, which assists locating the touch point precisely. This was realized at the device level by a cross-channel synaptic transistor in which the excitation of one conductive channel attenuates the other channel, improve the contrast in sensing the touch point, which is simultaneously displayed visually. The cross-shaped channels were fabricated using electro-hydrodynamic nanowire printing process to ensure scalable production of the array. Varying the intensity of the voltage input to the inhibitory channel laterally decreases the synaptic weight in the output channel, effectively simulating the contralateral inhibitory function at the device level. The device successfully assisted the location of touch by dealing with tactile information, and drive simultaneous display of the position. The special architecture of the device is applicable to develop a lateral-inhibition key for high-efficient Morse code encryption with 100% decryption accuracy. This work provides an innovative approach for designing and regulating intricate functionalities in the field of biomimetics and bioelectronics.

Methods

e-NWP of IZO NWs

Zinc acetate dihydrate ($Zn(CH_3COO)_2{\cdot}2H_2O$, ZnACD, metallic precursors), indium nitratehydrate ($In(NO_3)_3{\cdot}xH_2O$, InNH, metallic precursors) and polyvinyl pyrrolidone (PVP, sacrificial polymer) were dissolved in a mixture of N,N-dimethylformamide (DMF, common solvent) and chlorobenzene, and then stirring for 12 h at room temperature. Crossed IZO NW arrays were printed on the heat-resistant polyimide (PI) substrate. The distance between PI substrate and nozzle tip was set to 3 mm, and the electric field generated between the nozzle and the collector was 1 kV. The blended NWs were converted to IZO NWs by calcination in a muffle furnace at 450 °C in air.

Fabrication of CST

A pair of templated 80-nm gold source and drain electrodes was evaporated on the NWs. Ion gel was fabricated from poly(vinylidene fluoride-hexafluoropropylene) (P(VDF-HFP)) block copolymer and 1-ethyl-3-methylimidazolium bis(trifluoromethyl sulfonyl) imide ([EMIM]-[TFSI]) that covered on the IZO channel and part of the source and drain electrodes. A Pt probe was in contact with the ion gel sheet as the shared presynaptic input terminal.

Characterization. The morphological structure of NWs and were observed using a FEI Apreo S microscope. The arrangement of IZO NWs arrays was simply observed using the Leica DM2700M optical microscope (OM). Atomic force microscopy (AFM) images and height profiles of the 2D materials were collected using a Bruker dimension icon microscope operated in tapping mode. High-resolution transmission electron microscopy (HRTEM) images were obtained using a FEI Talos F200X microscope. Elemental mapping was acquired using a built-in Energy-dispersive X-ray spectroscopy (EDXS) measurement module in the TEM system. All electrical measurements were obtained using a Keithley 4200 SCS semiconductor analyzer in an N_2-filled glove box.

Fabrication of artificial tactile nervous system

The artificial tactile nervous system comprises an information processing unit and a signal acquisition and display unit. Information Processing Unit: A matrix thin-film pressure sensor (IMM00092A, i-Motion sensor) serves as the pressure-sensing module, whose electrical resistance (R_{sensor}) decreases with increasing applied pressure. R_{sensor} is connected in series with a voltage divider resistor (R_s). Consequently, the drain voltage (V_{DS2}) of the synaptic transistor increases/decreases as R_{sensor} increases/decreases. The two output currents (I_{out1} and I_{out2}) from the artificial synaptic device are converted into corresponding output voltages (V_{out1} and V_{out2}) using operational amplifiers (LM358). Signal Acquisition and Display Unit: A microcontroller unit (MCU, ATmega328P, Microchip) digitizes the analog signals V_{out1} and V_{out2}. Subsequently, these digital signals undergo threshold comparison. The results of this threshold comparison are then converted into voltage signals and transmitted to the liquid crystal display screen (ILI9431) for visualization.

Data availability

The data generated in this study are provided in the Source Data file and any additional data are available from the corresponding author upon request. Source data are provided with this paper.

References

1. Abraira, V. E. et al. The sensory neurons of touch. *Neuron* **79**, 618–639 (2013).
2. Perl, E. R. Myelinated afferent fibres innervating the primate skin and their response to noxious stimuli. *J Physiol* **197**, 593–615 (1968).
3. Brown, A. G. et al. Responses of spinocervical tract neurones to natural stimulation of identified cutaneous receptors. *Exp. Brain Res.* **7**, 231 (1969).
4. Johansson, R. S. et al. First spikes in ensembles of human tactile afferents code complex spatial fingertip events. *Nat. Neurosci.* **7**, 170–177 (2004).
5. Basbaum, A. I. et al. Cellular and molecular mechanisms of pain. *Cell* **139**, 267–284 (2009).
6. Scheibert, J. et al. The role of fingerprints in the coding of tactile information probed with a biomimetic sensor. *Science* **323**, 1503–1506 (2009).
7. Sugiura, Y. et al. Central projections of identified, unmyelinated (C) afferent fibers innervating mammalian skin. *Science* **234**, 358–361 (1986).

8. Luo, L. Architectures of neuronal circuits. *Science* **373**, eabg7285 (2021).
9. Arber, S. et al. Connecting neuronal circuits for movement. *Science* **360**, 1403–1404 (2018).
10. Fadok, J. P. et al. A competitive inhibitory circuit for selection of active and passive fear responses. *Nature* **542**, 96–100 (2017).
11. Koyama, M. et al. Mutual inhibition of lateral inhibition: a network motif for an elementary computation in the brain. *Curr. Opin. Neurobiol.* **49**, 69–74 (2018).
12. Obermayer, J. et al. Lateral inhibition by Martinotti interneurons is facilitated by cholinergic inputs in human and mouse neocortex. *Nat. Commun.* **9**, 4101 (2018).
13. Ratliff, F. et al. Enhancement of flicker by lateral inhibition. *Science* **158**, 392–393 (1967).
14. Olsen, S. R. et al. Lateral presynaptic inhibition mediates gain control in an olfactory circuit. *Nature* **452**, 956–960 (2008).
15. Macknik, S. L. et al. The spatial and temporal effects of lateral inhibitory networks and their relevance to the visibility of spatiotemporal edges. *Neurocomputing* **58-60**, 775–782 (2004).
16. Zhou, Y. et al. Role of lateral inhibition on visual number sense. *Front. Comput. Neurosci.* **16**, 810448 (2022).
17. Miller, P. Stimulus number, duration and intensity encoding in randomly connected attractor networks with synaptic depression. *Front. Comput. Neurosci.* **7**, 1–13 (2013).
18. Mira, J. et al. Knowledge modelling for the motion detection task: the algorithmic lateral inhibition method. *Expert Syst. Appl.* **27**, 169–185 (2004).
19. Fernández-Caballero. et al. A historical perspective of algorithmic lateral inhibition and accumulative computation in computer vision. *Neurocomputing* **74**, 1175–1181 (2011).
20. Fu, Q. et al. A parallel spiking neural network based on adaptive lateral inhibition mechanism for objective recognition. *Comput. Intell. Neurosci.* **4242235**, 14 (2022).
21. Delgado, A. E. et al. Real-time motion detection by lateral inhibition in accumulative computation. *Eng. Appl. Artif. Intel.* **23**, 129–139 (2010).
22. Cao, R. et al. Compact artificial neuron based on anti-ferroelectric transistor. *Nat. Commun.* **13**, 7018 (2022).
23. Han, J. K. et al. Artificial olfactory neuron for an in-sensor neuromorphic nose. *Adv. Sci.* **9**, 2106017 (2022).
24. Han, J. K. et al. Bioinspired photoresponsive single transistor neuron for a neuromorphic visual system. *Nano Lett* **20**, 8781–8788 (2020).
25. Zimmerman, A. et al. The gentle touch receptors of mammalian skin. *Science* **21**, 950–954 (2014).
26. Arslanova, I. et al. Somatosensory evoked potentials indexing lateral inhibition are modulated according to the mode of perceptual processing: comparing or combining multi-digit tactile motion. *Cogn. Neurosci.* **13**, 47–59 (2020).
27. Bodmer, B. et al. On the dependence of response inhibition processes on sensory modality: response inhibition processes and sensory modality. *Hum. Brain Mapp.* **38**, 1941–1951 (2017).
28. Min, S.-Y. et al. Large-scale organic nanowire lithography and electronics. *Nat. Commun.* **4**, 1773 (2013).
29. Conner, J. M. et al. Modulation of tactile feedback for the execution of dexterous movement. *Science* **374**, 316–323 (2021).
30. Nahmad-Rohen, L. et al. Contrast sensitivity and behavioural evidence for lateral inhibition in octopus. *Bio. Lett.* **15**, 20190134 (2019).
31. Atluri, P. P. et al. Determinants of the time course of facilitation at the granule cell to Purkinje cell synapse. *J. Neurosci.* **16**, 5661–5671 (1996).
32. Wang, L. et al. Human somatosensory processing and artificial somatosensation. *Cyborg Bionic Syst.* **2021**, 2692–7632 (2021).
33. Papaleonidopoulos, V. et al. β-adrenergic receptors reduce the threshold for induction and stabilization of LTP and enhance its magnitude via multiple mechanisms in the ventral but not the dorsal hippocampus. *Neurobiol. Learn. Mem.* **151**, 71–84 (2018).
34. López, J. C. A fresh look at paired-pulse facilitation. *Nat. Rev. Neurosci.* **2**, 307 (2001).
35. Bie, R. et al. Tunable neuromorphic computing for dynamic multi-timescale sensing in motion recognition. *Cyborg Bionic Syst* **6**, 0412 (2025).
36. Zucker, R. S. et al. Short-term synaptic plasticity. *Annu. Rev. Physiol.* **64**, 355–405 (2002).
37. Mathur, M. C. et al. Integrating physical system-theoretic and entropy-maximizing approaches of transport analysis. *Int. J. Syst. Sci.* **19**, 803–823 (1988).
38. Ni, Y. et al. Flexible organic artificial synapse with ultrashort-term plasticity for tunable time-frequency signal processing. *Chin. Chem. Lett.* **34**, 108419 (2023).
39. Kang, Y. H. et al. Facile preparation of highly conductive metal oxides by self-combustion for solution-processed thermoelectric generators. *ACS Appl. Mater. Inter.* **8**, 5216–5223 (2016).
40. Abbott, L. F. et al. Synaptic computation. *Nature* **431**, 796–803 (2004).
41. Yang, F. et al. Vertical-organic-nanocrystal-arrays for crossbar memristors with tuning switching dynamics toward neuromorphic computing. *SmartMat* **2**, 99–108 (2021).
42. He, B. et al. Frame-channel engineered multimodal transistor integrating neuromorphic computing with cross-modal edge intelligence. *Adv. Funct. Mater.* **35**, 2506332 (2025).
43. Hu, M. et al. A non-linear two-dimensional float gate transistor as a lateral inhibitory synapse for retinal early visual processing. *Mater. Horiz.* **9**, 2335–2344 (2022).
44. Liu, X. et al. Heterointerface-modulated synthetic synapses exhibiting complex multiscale plasticity. *Adv. Sci.* **12**, e17237 (2025).
45. Hu, Z. et al. The optoelectronic synergistic properties based on indium-gallium-zinc oxide neuromorphic transistors. *Nanotechnology* **36**, 235703 (2025).
46. Tan, H. et al. Tactile sensory coding and learning with bio-inspired optoelectronic spiking afferent nerves. *Nat. Commun.* **11**, 1369 (2020).
47. Wang, Z. et al. Polarization-sensitive artificial optoelectronic synapse based on anisotropic β-Ga_2O_3 single crystal for neuromorphic vision systems and information encryption. *Adv. Optical Mater.* **12**, 2401256 (2024).
48. Li, Y. et al. Vertical ion-coupling Ga_2O_3 TFT with spatiotemporal logic encryption. *IEEE T. Electron Dev.* **70**, 3122–3125 (2023).
49. Xiao, Y. et al. Functional integration of handwritten digit recognition and encryption/decryption based on Pt/GaO_x/TiN memristor array for a new data security system. *Ceram. Int.* **50**, 8981–8986 (2024).
50. Gao, K. et al. Biomaterial/organic heterojunction based memristor for logic gate circuit design, data encryption, and image reconstruction. *Adv. Funct. Mater.* **34**, 2401132 (2023).
51. Gong, F. et al. Reconfigurable logic and in-sensor encryption operations in an asymmetrically tunable van der Waals heterostructure. *Nano Res.* **17**, 3113–3119 (2023).
52. Cao, A. et al. A polar-switchable and controllable negative phototransistor for information encryption. *Mater. Horiz.* **10**, 5099–5109 (2023).
53. Mao, S. et al. Dual-modal artificial synapse based on a lead-free halide Cu_2AgBiI_6 for image processing and information encryption. *Chem. Eng. J.* **472**, 145086 (2023).
54. Hu, L. et al. In situ cryptography in a neuromorphic vision sensor based on light-driven memristors. *Appl. Phys. Rev.* **11**, 011411 (2024).
55. Zhu, X. et al. Negative phototransistors with ultrahigh sensitivity and weak-light detection based on 1D/2D molecular crystal p–n heterojunctions and their application in light encoders. *Adv. Mater.* **34**, 2201364 (2022).

Acknowledgements
This work was supported in part by the National Science Fund for Distinguished Young Scholars of China (T2125005) (W.X.), the National Key R&D Program of China (2022YFA1204500, 2022YFA1204504) (W.X.), and the Postdoctoral Fellowship Program (GZC20250363) (L.L.).

Author contributions
W.X. conceived the work. L.L. and W.X. constructed the research frame. L.L. and Y.N. prepared the devices. H.X. designed the external circuit of artificial tactile nervous system. Y.Y. did the simulation. L.L., Y.N. and H.X. performed the data and wrote the manuscript. W.X. directed the project. All authors discussed the results and implications and commented on the manuscript at all stages.

Competing interests
The authors declare no competing interests.

Additional information
Supplementary information The online version contains supplementary material available at https://doi.org/10.1038/s41467-025-68139-9.

Correspondence and requests for materials should be addressed to Wentao Xu.

Peer review information *Nature Communications* thanks the anonymous reviewers for their contribution to the peer review of this work. A peer review file is available.